Biosensors and Bioelectronics 78 (2016) 497–504

Contents lists available at ScienceDirect

Biosensors and Bioelectronics

journal homepage: www.elsevier.com/locate/bios

Nanostructured zirconia decorated reduced graphene oxide based efficient biosensing platform for non-invasive oral cancer detection

Suveen Kumar, Jai Gopal Sharma, Sagar Maji, Bansi Dhar Malhotra *

Nanobioelectronics Laboratory, Department of Biotechnology, Delhi Technological University, Delhi 110042, India

ARTICLE INFO

Article history:
Received 15 September 2015
Received in revised form
13 November 2015
Accepted 27 November 2015
Available online 30 November 2015

Keywords:
Biosensor
Zirconia
Reduced graphene oxide
CYFRA-21-1
Oral cancer

ABSTRACT

We report results of the studies relating to fabrication of a non-invasive, label-free and an efficient biosensing platform for detection of the oral cancer biomarker (CYFRA-21-1). One step hydrothermal process was used for uniform decoration of nanostructured zirconia (average particle size 13 nm) on reduced graphene oxide (ZrO_2–RGO) to avoid coagulation of the zirconia nanoparticles and to obtain enhanced electrochemical performance of ZrO_2–RGO nanocomposite based biosensor. Further, ZrO_2–RGO has been functionalized using 3-aminopropyl triethoxy saline (APTES) and electrophoretically deposited on the indium tin oxide coated glass substrate at a low DC potential.The APTES/ZrO_2–RGO/ITO electrode exhibits improved heterogeneous electron transfer (more than two times) with respect to that of the APTES/ZrO_2/ITO electrode indicating faster electron transfer kinetics. The –NH_2 containing APTES/ZrO_2–RGO/ITO platform is further biofunctionalized with anti-CYFRA-21-1. The structural and morphological investigations of the ZrO_2–RGO based biosensing platform have been accomplished using X-ray diffraction (XRD), electrochemical, transmission electron microscopy (TEM), atomic force microscopy (AFM) and Fourier transform infrared spectroscopy (FT-IR) studies. This immunosensor exhibits a wider linear detection range (2–22 ng mL^{-1}), excellent sensitivity (0.756 μA mL ng^{-1}) and a remarkable lower detection limit of 0.122 ng mL^{-1}. The observed results have been validated via enzyme linked immunosorbent assay (ELISA).

1. Introduction

Non-invasive detection strategy is considered to be a promising alternative for detection of human diseases (Guilbault et al., 1995). To accomplish this, saliva, tear, urine and sweat have been proposed as interesting for desired biomedical investigations (Chen et al., 2011; Tille, 2013). Among these, saliva based clinical testing has many advantages due to easier saliva collection, low cost of storage and easy transport (Lawrence, 2002). Further, the non-invasive saliva based collection techniques can dramatically reduce anxiety and discomfort for monitoring disease and general health of a patient. Saliva is a useful non-invasive body fluid that can be used for biomarker detection. Besides this, it is one of the simplest and easily accessible body fluid that can be utilized for a wide range of applications including early detection and monitoring of diseases including oral cancer (Lawrence, 2002; Tille, 2013).

Oral cancer (OC) is currently the sixth most common cancer and is caused by uncontrolled growth of cells in the floor of mouth, lips, sinuses, tongue, cheeks, throat etc. (Kujan et al., 2006; Kumar et al., 2015a). The main reasons behind this cancer are chewing of tobacco, smoking, alcohol consumption, gastro-esophageal reflux disease, human papillomavirus and exposure to chemicals (e.g. formaldehyde and asbestos) (Gorschinski et al., 2009). These high risk factors may alter the expression of p16, APC and p53 genes resulting in the origin of oral cancer (Gonzalez et al., 1997). This cancer can be life threatening if not detected and is not treated at an early stage. For diagnosis of the oral cancer, laser-capture micro-dissection, visualization adjuncts, cytopathology and biopsy techniques can be used and these techniques require tissue specimens that are highly painful to obtain (Mehrotra and Gupta, 2011; Patton et al., 2008; Scully et al., 2008). Besides this, these methods are highly expensive, time consuming and require skilled personnel for specimen collection. However, the non-invasive biosensing is attractive, cost effective, accurate and easier to use for oral cancer detection (Malhotra et al., 2012; Mehrotra and Gupta, 2011; Scully et al., 2008).

The salivary biomarkers such as Interleukin-8 (IL-8), Interleukin-6 (IL-6), Interleukin-1 (IL-1), Interleukin-1β (IL-1β), TNFα-1, Endotheline-1 (ET-1), HNP-1, hsa-miR-200a can be used for early diagnosis and prognosis of the oral cancer (Malhotra et al., 2010; Pickering et al., 2007; Punyani and Sathawane, 2013). However,

* Corresponding author.
E-mail address: bansi.malhotra@gmail.com (B.D. Malhotra).

http://dx.doi.org/10.1016/j.bios.2015.11.084
0956-5663/

only a few reports are available for detection of salivary biomarkers using biosensing technique. Most of these biomarkers are secreted in very low amount (pg mL^{-1}) (Malhotra et al., 2012, 2010; Mehrotra and Gupta, 2011). CYFRA-21-1, a proteinaceous biomarker (also known as cytokeratin-19) is a member of keratin family that is known to maintain structural integrity of the epithelial cells. It is a 40 kDa molecule encoded by *KRT19* gene. In saliva of oral cancer patients, it is secreted in higher concentration (17.46 ± 1.46 ng mL^{-1}) (Nagler et al., 2006; Rajkumar et al., 2015).

Transducers are known to play an important role towards the fabrication of an efficient biosensor. It provides an interactive platform for the immobilization of biomolecules on desired substrate and can be used for monitoring of an electrical signal resulting due to an electrochemical reaction at an electrode surface, usually as a result of an imposed potential, current or frequency. The unique properties of a transducer can be helpful in improving the characteristics of a biosensor (Roushani and Valipour, 2016; Solanki et al., 2011). Nanostructured metal oxides (NMOs) have been found to have interesting optical and electrical properties due to electron and phonon confinement, high surface-to-volume ratio, modified surface work function, high surface reaction activity, high catalytic efficiency and strong adsorption ability. The NMOs can thus be utilized for increased loading of desired biomolecules per unit mass of particles. Among the various NMOs, zirconia has been found to have interesting physiochemical as well as biosensing characteristics (Das et al., 2011). Biocompatibility, excellent electrical and surface charge properties, oxygen moieties in ZrO_2 make it a promising material as a transducer in the fabrication of a biosensor (Das et al., 2011; Liu and Lin, 2005; Kumar et al., 2015a). In this context, it has been reported that zirconia nanoparticles tend to aggregate and form large clusters (Kumar et al., 2015a; Zhao et al., 2006). To overcome these problems, a substrate material with a high surface area and good conductivity is crucial for increasing the physiochemical and biosensing activity of zirconia nanoparticles.

The chemically reduced graphene oxide (GO) has recently been found to be a promising substrate for uniform distribution of metal oxide nanoparticles (Dong et al., 2012; Sawangphruk et al., 2013; Wei et al., 2011). The reduced graphene oxide (RGO) has been demonstrated to have excellent electrochemical conductivity due to rapid heterogeneous electron transport (HET), superior mechanical flexibility and remarkable stability that can be helpful for the fabrication of an efficient biosensing platform (Ali et al., 2014). Gong et al. (2012) proposed a facile electrochemical approach for synthesis of zirconia–reduced graphene oxide nanosheets for application in enzyme less methyl parathion sensor. Efforts have also been made to detect hydroquinone and catechol using RGO–ZrO_2 based sensor (Vilian et al., 2014).

We report for the first time results of the studies relating to application of zirconia decorated reduced graphene oxide nanocomposite as a transducer for development of an immunosensor. This immunosensor can be used for non-invasive, label-free and efficient detection of oral cancer biomarker (CYFRA-21-1) and it covers the entire physiological range (3.8 to17.46 ± 1.46 ng mL^{-1}) secreted in saliva of oral cancer patients. The results obtained have been validated via enzyme linked immunosorbent assay (ELISA).

2. Materials and methods

2.1. Chemicals

Zirconium ethoxide, natural graphite flakes and 1-(3-(dimethylamino)-propyl)-3-ethylcarbodiimide hydrochloride (EDC) were purchased from Sigma-Aldrich. Sodium hydroxide, cetyltrimethylammonium bromide (CTAB), sodium monophosphte, sodium diphosphate dihydrate and N-hydroxysuccinimide (NHS) were purchased from Fisher Scientific. 3-aminopropyl triethoxy saline (APTES) was purchased from Alfa-aesar. All the chemicals were of analytical grade and used without any further purification. Electrochemical studies were performed using 0.05 M phosphate buffer solution (PBS) prepared using sodium monophosphte and sodium diphosphatedihydrate. All solutions prepared using milli-Q water having resistivity of 18 MΩ cm were stored at 4 °C. CYFRA-21-1 antigen and anti-CYFRA-21-1 antibodies were purchased from Ray Biotech, Inc., India. These biomolecules were further diluted by using PBS buffer of pH 7.0. CYFRA-21-1 ELISA Kit was purchased from Kinesis DX, USA.

2.2. Fabrication of biosensing platform

Nanostructured ZrO_2 decorated RGO was prepared and functionalized with APTES (please see Supporting Information). 20 mg of functionalized nanocomposite (APTES/ZrO_2–RGO) was dispersed in 50 mL of acetonitrile by mild ultrasonication. The electrophoretic deposition (EPD) technique was used to deposit thin film of APTES/ZrO_2–RGO onto prehydrolyzed ITO glass that worked as an anode and platinum wire as cathode, placed parallely at a separation distance of 1 cm in glass cell. These were dipped in the prepared colloidal solution and electrophoretically deposited at an optimized DC potential (15 V) for about 3 min using electrophoretic deposition unit (Genetix, GX300C). This APTES/ZrO_2-RGO/ITO film was washed with deionized water and dried at room temperature (25 °C) over night. Next, a stock solution (50 μg mL^{-1}) of anti-CYFRA-21-1 was prepared in PBS (pH = 7.0). For activation of the –COOH groups of antibodies, EDC–NHS chemistry was used where EDC (0.2 M) worked as a coupling agent and NHS (0.05 M) as an activator. A solution mixture of anti-CYFRA-21-1, EDC and NHS in 2:1:1 ratio was made and kept at room temperature (25 °C) for 30 min. Further, 30 μL of activated antibody solution was uniformly spread over APTES/ZrO_2–RGO/ITO electrode and kept in a humid chamber at room temperature (25 °C) during the next 3 h. Thereafter, it was washed with PBS to remove any unbound antibody molecules. 20 μL of BSA (2 mg dL^{-1}) was used for blocking the non-specific active sites. The fabricated BSA/anti-CYFRA-21-1/APTES/ZrO_2–RGO/ITO immunoelectrode was washed with PBS and stored at 4 °C until further use.

2.3. Sample collection and processing

Saliva samples of eight OC patients were collected from Rajiv Gandhi Cancer Institute and Research Centre (RGCIRC), Delhi (India) after written consent by the patients. Prior to this,we took ethical approval of the Institutional Review Board of RGCIRC and Institutional Ethical and Biosafety Committee, DTU. We collected un-stimulated saliva samples after rinsing the mouth with 5 mL deionized water and thereafter expectorated into sterilized tube. These samples were centrifuged at 2800 rcf (25 °C) for 30 min. the supernatant was collected in sterilized eppendorf and stored at −20 °C until further use (Rajkumar et al., 2015). All the samples were collected, processed and stored in a similar fashion.

3. Results and discussion

3.1. X-ray diffraction (XRD) and Electron microscopy studies

Fig. 1a shows the XRD pattern obtained for the hydrothermally synthesized ZrO_2–RGO nanocomposite. The peak observed at 24.2° is due to merging of the ZrO_2 (110) and RGO (002) planes. Further, the relatively lower intensity broad peak is observed at 43.0°

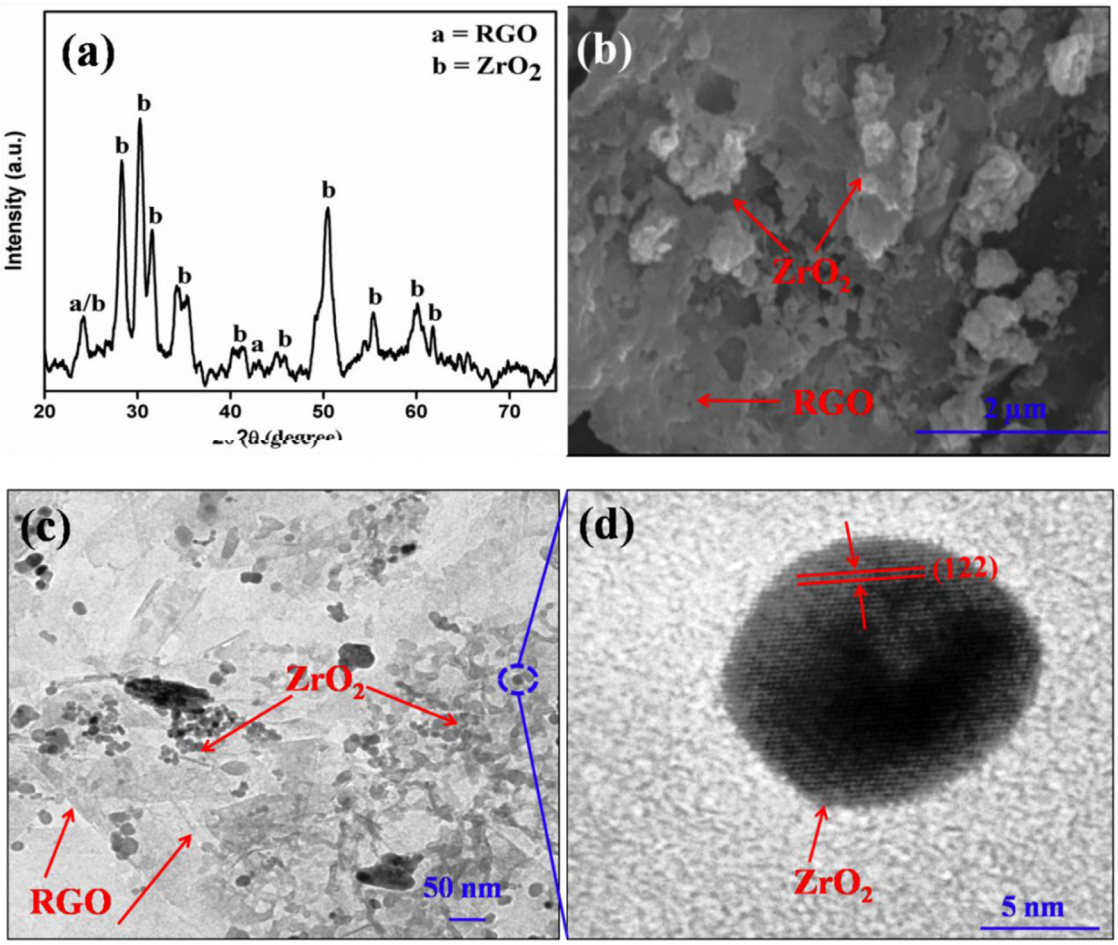

Fig. 1. (a) XRD pattern (b) SEM and (c) TEM image of ZrO_2 grafted reduced graphene oxide (d) HR-TEM image of individual ZrO_2.

indicating RGO planes of (001) (Srivastava et al., 2013). The other reflection peaks observed at 28.34°, 30.28°, 31.6°, 34.2°, 35.4°, 40.3°, 44.9°, 50.4°, 55.3°, 60.1° and 61.8° correspond to (111), (111), (−111), (022), (200), (−102), (−211), (122), (013), (302) and (−113) planes. These results indicate grafting of the pure monoclinic phase of ZrO_2 (Kumar et al., 2015a) on the surface of RGO sheet. The average grain size (D) of the grafted zirconia on RGO surface is found to be 13 nm, calculated using Scherrer formula i.e. $D=0.94\lambda/\beta\cos\theta$, where λ (=1.54060 Å) is the X-ray wavelength, β is the full width at half maximum and θ is the Bragg angle.

Fig. 1b–d shows SEM, TEM and HR-TEM images of the synthesized ZrO_2–RGO nanocomposite. A well dispersed solution of ZrO_2–RGO nanocomposite is prepared in milli-Q water and dropped onto 50 mesh carbon coated gold grid and dried at room temperature for the TEM studies. It appears that spherical ZrO_2 nanoparticles are uniformly grafted on the RGO sheet (Fig. 1b and c). Fig. 1d shows an individual spherical ZrO_2 nanoparticle present at the RGO sheet indicating a crystal lattice spacing of 0.179 nm corresponding to the inter-spacing of the (122) plane with an average grain size of 13 nm. The calculated grain size of ZrO_2 is in

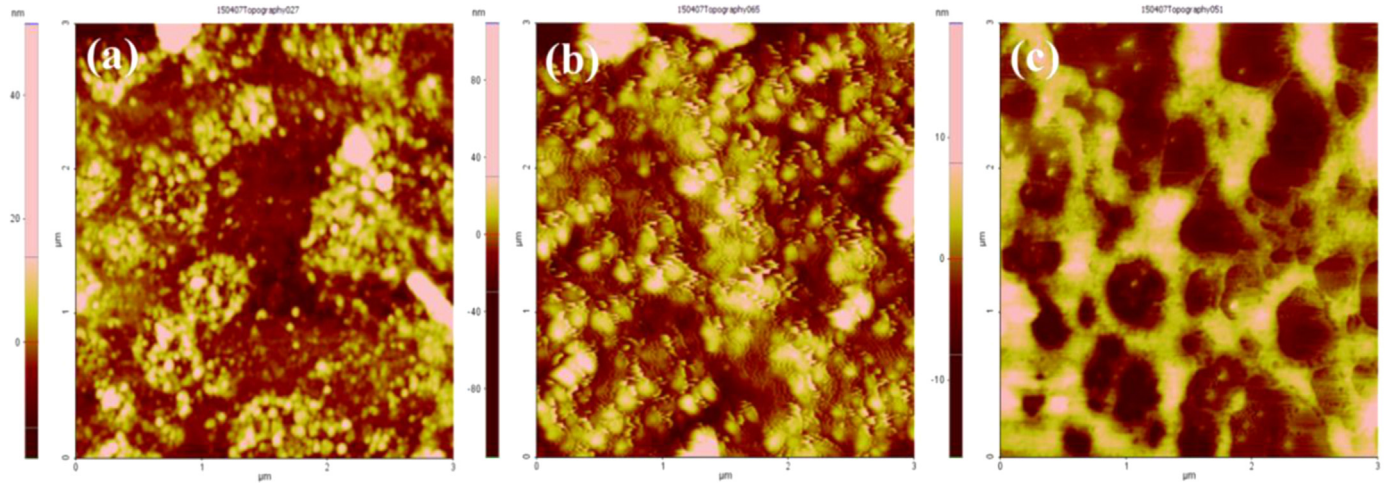

Fig. 2. Atomic force microscopic images of (a) APTES/ZrO_2–RGO/ITO (b) anti-CYFRA/APTES/ZrO_2–RGO/ITO and (c) BSA/anti-CYFRA/APTES/ZrO_2–RGO/ITO electrodes.

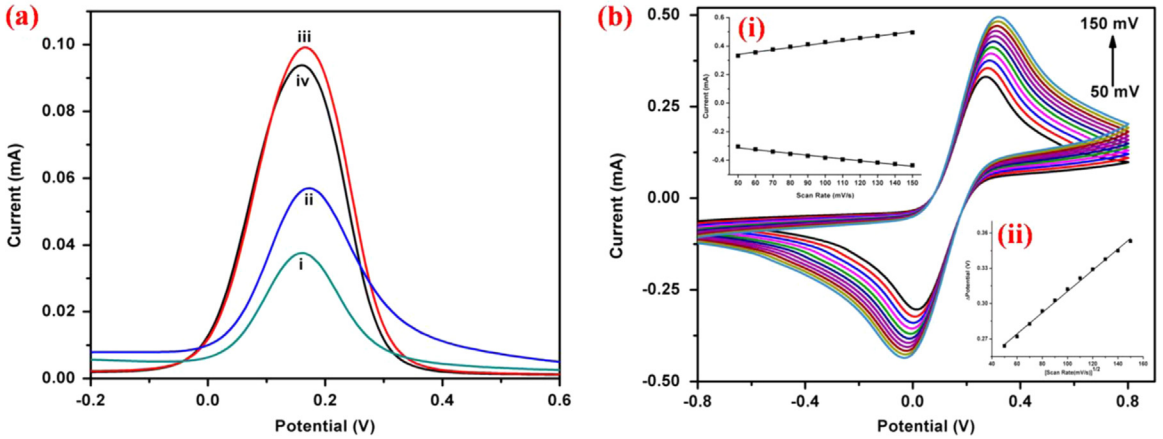

Fig. 3. (a) Electrode response study of APTES/ZrO_2/ITO (curve i), APTES/ZrO_2–RGO/ITO (curve ii), anti-CYFRA-21-1/APTES/ZrO_2–RGO/ITO (curve iii) and BSA/anti-CYFRA-21-1/APTES/ZrO_2–RGO/ITO (curve iv) and (b) scan rate studies of BSA/anti-CYFRA-21-1/APTES/ZrO_2–RGO/ITO [inset (a) magnitude of oxidation and reduction current generated as response of scan rate (mV/s), inset (b) potential as function of scan rate] electrodes.

support of the results of X-ray diffraction studies (Fig. 1a)

3.2. Atomic force microscopic (AFM) studies

Fig. 2 shows AFM image of (a) APTES/ZrO_2–RGO/ITO, (b) anti-CYFRA-21-1/APTES/ZrO_2–RGO/ITO and (c) BSA/anti-CYFRA-21-1/APTES/ZrO_2–RGO/ITO obtained in the non-contact mode. The average roughness of APTES/ZrO_2–RGO/ITO electrode is observed to be 4.256 nm with granular topography, indicating uniform electrophoretic deposition of functionalized ZrO_2–RGO film on ITO coated glass electrode. After covalent immobilization of anti-CYFRA-21-1, topography of the electrode changes from granular to globular as shown in Fig. 2 (b). The average roughness increases to 27.803 nm and the observed globular topography reveals successive immobilization of biomolecules on the APTES/ZrO_2–RGO/ITO electrode. Fig. 2(c) shows that the average roughness of the electrode decreases to 1.521 nm after BSA immobilization. This can be attributed to blocking of the non-specific binding sites and formation of highly uniform immunoelectrode surface.

3.3. Fourier transform infrared spectroscopy (FT-IR)

FT-IR studies have been carried out to investigate the presence of functional groups on fabricated APTES/ZrO_2–RGO/ITO electrode and bond formation after immobilization on anti-CYFRA-21-1. Fig. S1 (Supplementary information) shows FT-IR spectra of (i) APTES/ZrO_2–RGO/ITO and (ii) anti-CYFRA-21-1/APTES/ZrO_2–RGO/ITO. In spectra (i) the peak at 1099 cm^{-1} is due to the C–OH stretching vibration present on the RGO sheet. The band found at 1557 cm^{-1} is due to the bending vibration mode of the secondary amide groups. The bands present at 1641 cm^{-1} and 3350 cm^{-1} are due to bending mode of primary amide groups indicating presence of the free $-NH_2$ groups on surface of APTES/ZrO_2–RGO/ITO electrode. The additional peaks observed at 2852 cm^{-1} and 2922 cm^{-1} are attributed to C–H bonds of alkanes and aldehydes groups present on the APTES molecules as well as on RGO sheet (Ali et al., 2014). In spectra (ii) an additional broad band is observed between 1220 and 1300 cm^{-1} indicating amide bond (C–N) formation between $-NH_2$ groups present on APTES/ZrO_2–RGO/ITO electrode and –COOH groups present in Fc region of anti-CYFRA-21-1 biomolecules revealing successful covalent immobilization of the anti-CYFRA-21-1 (Ali et al., 2014). The peaks seen at 1269 cm^{-1}, 1452 cm^{-1}, 1562 cm^{-1}, 1641 cm^{-1} and 2712 cm^{-1} can be assigned to C–O, C=C, $-NH_2$ (primary amine), –NH-R (secondary amine) and C–H groups of aldehydes, respectively (Ali et al., 2014; Pasternack et al., 2008; Vasudev et al., 2013). In both spectra (i) and (ii), a sharp peak with the same intensity is observed at 2360 cm^{-1} due to presence of O–H groups of carboxylic acid present on RGO. This indicates that anti-CYFRA-21-1 is not bound with carboxylic acid of RGO present on APTES/ZrO_2–RGO/ITO electrodes.

3.4. Electrochemical studies

Fig. S2 shows the effect of $[Fe(CN)_6]^{3-/4-}$ on CV of APTES/ZrO_2–RGO/ITO and BSA/anti-CYFRA-21-1/APTES/ZrO_2–RGO/ITO electrodes.) It can be seen (Fig. S2(a) and (b)) that in the presence of $[Fe(CN)_6]^{3-/4-}$, cyclic voltammogram shows oxidation as well as reduction peaks. In the absence of $[Fe(CN)_6]^{3-/4-}$, we did not observe any redox peak current in case of the APTES/ZrO_2–RGO/ITO and BSA/anti-CYFRA-21-1/APTES/ZrO_2–RGO/ITO electrodes. In the present studies, $[Fe(CN)_6]^{3-/4-}$ was used as an electron mediator that provides electronic amplification, facilitating high-sensitivity as a result of occurrence of each of the biomolecular complexation event.

Fig. S3 shows electrochemical response of the BSA/anti-CYFRA-21-1/APTES/ZrO_2–RGO/ITO immunoelectrode as a function of pH (6.0 to 8.0) in PBS buffer (50 mM, 0.9% NaCl) containing $[Fe(CN)_6]^{3-/4-}$ (5 mM) ions using differential pulse voltametry (DPV) technique. The DPV shows maximum peak current at pH 7.0. This is because at neutral pH , structure of the biological molecule is preserved (Liu and Lin, 2005). Thus PBS buffer with pH 7.0 was used for the electrochemical studies.

Fig. 3a shows DPV response of (i) APTES/ZrO_2/ITO (ii) APTES/ZrO_2–RGO/ITO (iii) anti-CYFRA-21-1/APTES/ZrO_2–RGO/ITO and (iv) BSA/anti-CYFRA-21-1/APTES/ZrO_2–RGO/ITO electrode at a scan rate of 50 mV/s in the potential range, −0.2 to 0.6 V. It is found that APTES/ZrO_2/ITO electrode exhibits a peak current of 0.037 mA and is 0.057 mA in case of the APTES/ZrO_2–RGO/ITO electrode. This is attributed to the excellent electrochemical properties of the reduced graphene oxides sheets present in the RGO–ZrO_2 composite. After immobilization of the antibodies, the anti-CYFRA-21-1/APTES/ZrO_2–RGO/ITO electrode shows increased peak current of 0.10 mA. The observed increase in the peak current after immobilization of anti-CYFRA-21-1 on APTES/ZrO_2–RGO/ITO electrode is due to presence of the ZrO_2–RGO matrix that acts as a mediator at the electrode surface (ITO) resulting in significant decrease of the electron tunneling distance between the antibodies and the electrode (Anusha et al., 2014; Vasudev et al., 2013). Besides this, presence of the electrostatic interaction between the free site of the antibodies ($-NH_2$ terminal) and the

redox species results in faster electron diffusion towards the immunoelectrode (Kumar et al., 2015b). BSA has been used for blocking the non-specific active sites of the anti-CYFRA-21-1/APTES/ZrO_2–RGO/ITO immunoelectrode. After BSA immobilization, magnitude of the peak current further decreases to 0.094 mA due to insulating nature of the BSA molecules (Kumar et al., 2015; Vilian et al., 2014). Further, impedance spectrum was measured in the frequency range, 100 kHz–100 mHz, with varying potential from 10 to 100 mV (Fig. S4). It is found that the impedance spectra changes shape as the voltage increases and with increase in the voltage there is a decrease in the charge transfer resistance (R_{ct}) value after 20 mV. Thus, 20 mV was selected as the optimized voltage for all the impedance measurements. To investigate the heterogeneous electron transport (HET) of APTES/ZrO_2/ITO and APTES/ZrO_2–RGO/ITO electrodes, electrochemical impedance spectroscopy (EIS) studies were conducted at 20 mV/s (Fig. S5). The HET (6.624×10^{-6} cm s^{-1}) of APTES/ZrO_2/ITO electrode is found to increase by more than two times (14.49×10^{-6} cm s^{-1}) when RGO is incorporated in APTES/ZrO_2–RGO/ITO electrode facilitating faster electron transfer.

The cyclic voltammogram (CV) of APTES/ZrO_2–RGO/ITO and BSA/anti-CYFRA-21-1/APTES/ZrO_2–RGO/ITO electrodes were recorded as a function of scan rate (50–150 mV/s) (Figs. S6 and 3b). The magnitudes of both anodic (Ipa) and cathodic (Ipc) peak currents exhibit a linear relationship with scan rate (Figs. S6 and 3b, inset a) indicating that the electrochemical reaction is a diffusion-controlled process (Vasudev et al., 2013) and follows Eqs. (1)–(4):

$$\mathrm{Ipc}_{(\mathrm{APTES/ZrO2-RGO/ITO})} = \left[1.43\times10^{-9}\ \mathrm{A(s/mV)}\times(\text{scan rate[mV/s]})^{1/2}\right] + 2.31\times10^{-7}\ \mathrm{A},\ R^2=0.99,\ \mathrm{SD}=4.53\times10^{-6} \quad (1)$$

$$\mathrm{Ipa}_{(\mathrm{APTES/ZrO2-RGO/ITO})} = -\left[1.25\ 10^{-9}\ \mathrm{A\ (s/mV)}\times(\text{scan rate[mV/s]})^{1/2}\right]-2.05\times10^{-7}\ \mathrm{A},\ R^2=0.99,\ \mathrm{SD}=4.11\times10^{-6} \quad (2)$$

$$\mathrm{Ipc}_{(\mathrm{BSA/anti\text{-}CYFRA-21-1/APTES/ZrO2-RGO/ITO})} = \left[1.60\times10^{-9}\ \mathrm{A(s/mV)}\times(\text{scan rate[mV/s]})^{1/2}\right] + 2.61\times10^{-7}\ \mathrm{A},\ R^2=0.99,\ \mathrm{SD}=4.53\times10^{-6} \quad (3)$$

$$\mathrm{Ipa}_{(\mathrm{BSA/anti\text{-}CYFRA-21-1/APTES/ZrO2-RGO/ITO})} = -\left[1.29\times10^{-9}\ \mathrm{A\ (s/mV)}\times(\text{scan rate[mV/s]})^{1/2}\right] -2.48\times10^{-7}\ \mathrm{A},\ R^2=0.99,\ \mathrm{SD}=4.11\times10^{-6} \quad (4)$$

Further it is observed that with increasing scan rate, the oxidation peak shifts towards higher potential and the reduction peak shifts towards lower potential. The linearity is obtained between the difference in magnitude of the oxidation peak potential and reduction peak potential ($\Delta V = V_{pa} - V_{pc}$, V_{pa} is anodic peak potential and V_{pc} is cathodic peak potential) as a function of scan rate (Fig. S6 and 3b, inset b), indicating facile charge transfer kinetics between medium to electrode (Kumar et al., 2015a) and follows Eqs. (5) and (6) :

$$\Delta V_{(\mathrm{APTES/ZrO2-RGO/ITO})} = \left[1.70\times10^{-3}\ \mathrm{V(s/mV)}\times(\text{scan rate[mV/s]})^{1/2}\right] + 0.346\ \mathrm{V},\ R^2=0.99,\ \mathrm{SD}=4.79\times10^{-3} \quad (5)$$

$$\Delta V_{(\mathrm{BSA/anti-CYFRA-21-1/APTES/ZrO2-RGO/ITO})} = \left[0.90\times10^{-3}\ \mathrm{V(s/mV)}\times(\text{scan rate[mV/s]})^{1/2}\right] + 0.220\ \mathrm{V},\ R^2=0.99,\ \mathrm{SD}=1.75\times10^{-3} \quad (6)$$

where R is the correlation coefficient and SD is the standard deviation. The diffusion coefficient (D) of BSA/anti-CYFRA-21-1/APTES/ZrO_2–RGO/ITO immunoelectrode has been determined to be 1.12×10^{-3} cm^2 s^{-1} using Randle Sevick equation (Sharma et al., 2012):

$$I_p = \left(2.69\times10^5\right) n^{3/2} A D^{1/2} C \upsilon^{1/2} \quad (7)$$

where I_p is the peak current of immunoelectrode, n is the number of electrons (1) transferred, A is the active surface area of the immunoelectrode (0.25 cm^2), D is the diffusion coefficient, C is the concentration of redox species (5×10^{-3} mol cm^{-2}) and υ is the scan rate (50 mV/s).

The surface concentration of BSA/anti-CYFRA-21-1/APTES/ZrO_2–RGO/ITO immunoelectrode has been calculated to be 8.03×10^{-9} mol cm^{-2} by using Laviron's theory (Sharma et al., 2012):

$$I_p = n^2 F^2 \gamma A \upsilon (4RT)^{-1} \quad (8)$$

where I_p represents the peak current of immunoelectrode, n is the number of electrons (1) transferred, F is the Faraday constant (96,485 C mol^{-1}), γ is the surface concentration of the absorbed electro-active species, A is the surface area of the electrode, ν is the scan rate (V/s), R is the gas constant (8.314 J mol^{-1} K^{-1}) and T is room temperature (25 °C or 298 K).

3.5. Response studies

Differential pulse voltammetry (DPV) technique has been utilized to investigate electrochemical response of the fabricated BSA/anti-CYFRA-21-1/APTES/ZrO_2–RGO/ITO immunoelectrode as a function of CYFRA-21-1 concentration in PBS buffer (50 mM, 0.9% NaCl) containing $[Fe(CN)_6]^{3-/4-}$ (5 mM) (Fig. 4b). It has been found that magnitude of the anodic peak current increases after formation of antigen–antibody complex between CYFRA-21-1 and anti-CYFRA-21-1 on the electrode surface. To investigate the reasons behind increased peak current, we analyzed the sequence of CYFRA-21-1 (Cytokeratin 19 fragments, *Homo sapiens*) obtained from NCBI protein database (Accession: AAF27048.1, shown in Fig. S7). It can be seen that CYFRA-21-1 protein contains 14 residues of tyrosine (Y) molecules. During an electrochemical reaction these tyrosine molecules undergo oxidation and release electrons (as shown in Scheme S1) resulting in increased peak current. (Okuno et al., 2007, Wei et al., 2012, Palecek et al., 2015) The increased concentration of amino acids due to increased concentration of CYFRA-21-1 antigen is likely to result in enhanced antigen–antibody interaction onto APTES/ZrO_2–RGO/ITO electrode leading to increased peak current. Alternatively, it may perhaps be attributed to both the conformation changes in the BSA/anti-Cyfra-21-1/APTES/ZrO_2–RGO matrix and the strong affinity of CYFRA-21-1 antigen towards the spatially oriented antibodies that are likely to provide easy conducting paths for electron transfer to the BSA/anti-CYFRA-21-1/APTES/ZrO_2–RGO/ITO electrode leading to improved sensing characteristics such as linearity, faster response time and shelf life (Wan et al., 2013, Okuno et al., 2007, Kaushik et al., 2009, Viswanathan et al., 2006, Zhang et al., 2008, Kumar et al., 2015b). The magnitude of anodic current increases with increasing concentration of CYFRA-21-1 from 2 to 22 ng mL^{-1} (Fig. 4d) after which the current tends to saturate at higher concentrations. All the experiments were repeated three times at each concentration. Results of the response studies

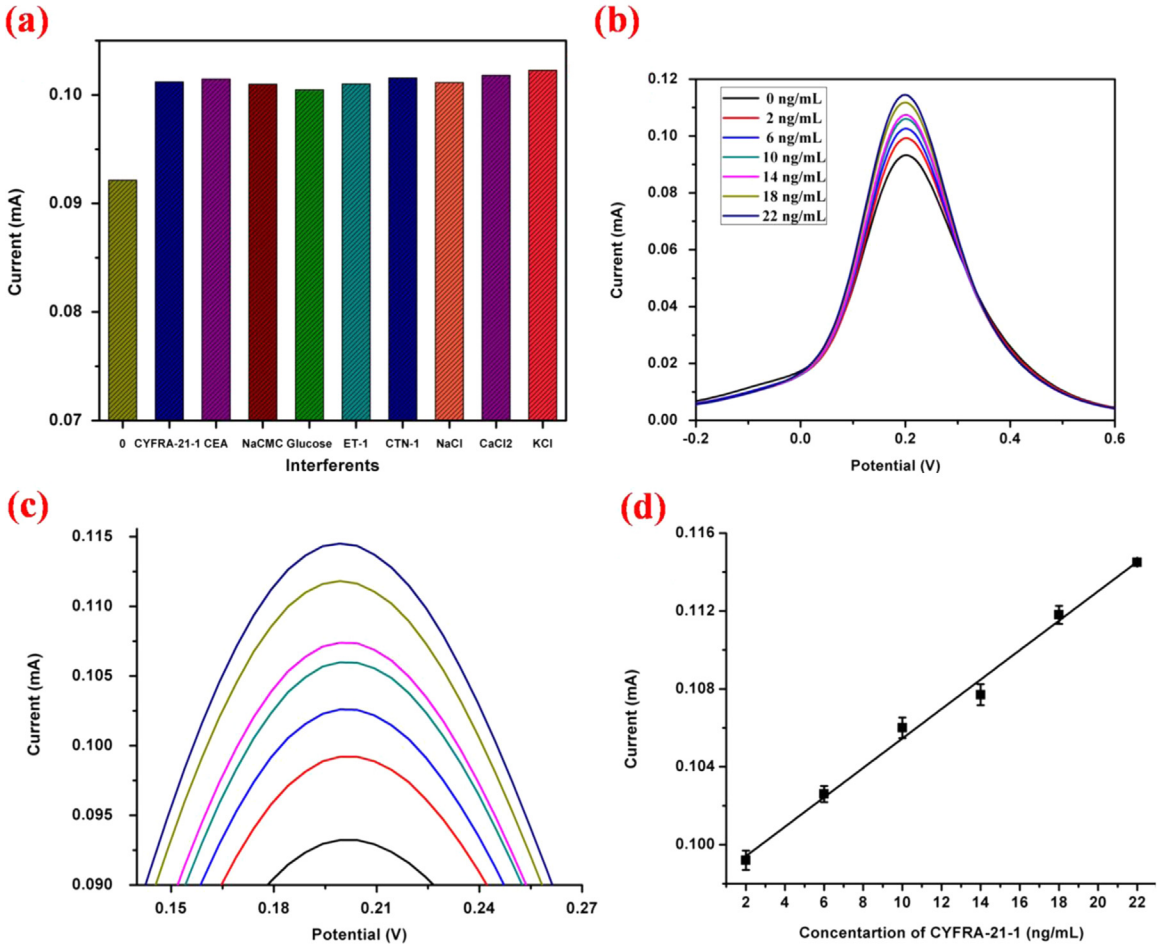

Fig. 4. (a) Interferents studies of BSA/anti-CYFRA-21-1/APTES/ZrO_2–RGO/ITO immunoelectrode (b) electrochemical response studies of BSA/anti-CYFRA-21-1/APTES/ZrO_2–RGO/ITO immunoelectrode as a function of CYFRA-21-1 concentration (2–22 ng/mL) (c) magnified view of oxidation peak current (d) a calibration curve has beet plotted between peak current and CYFRA-21-1 concentration.

indicate that BSA/anti-CYFRA-21-1/APTES/ZrO_2–RGO/ITO immunoelectrode can be used to detect CYFRA-21-1 in the range of 2–22 ng mL^{-1} (R^2=0.99). The sensitivity of the fabricated immunoelectrode can be estimated by the slope of the curve and is found to be 0.756 μA mL ng^{-1}. The standard deviation and limit of detection (LOD) for the immunoelectrode are obtained to be 3.08×10^{-5} and 0.122 ng mL^{-1}, respectively. The limit of detection has been calculated using the standard Eq. (9):

$$\text{Limit of detection} = 3\,\sigma/\text{Sensitivity} \quad (9)$$

where σ is standard deviation of the BSA/anti-CYFRA-21-1/APTES/ZrO_2–RGO/ITO immunoelectrode.

We conducted a control experiment using covalently immobilized anti-CYFRA-21-1 onto electrophoretically deposited RGO on ITO electrode. Fig. S8(a) shows the electrochemical response of the fabricated BSA/anti-CYFRA-21-1/RGO/ITO immunoelectrode as a function of CYFRA-21-1 concentration in PBS buffer (50 mM, 0.9% NaCl) containing $[Fe(CN)_6]^{3-/4-}$ (5 mM). It can be seen that the electrochemical response increases as a function of CYFRA-21-1 concentration (Fig. S8b). Similar behavior is observed in case of the APTES/ZrO_2 based immunosensor (Kumar et al., 2015b). And it may be noted that the observed results obtained in case of BSA/anti-CYFRA-21-1/RGO/ITO, BSA/anti-CYFRA-21-1/ZrO_2/ITO and BSA/anti-CYFRA-21-1/ZrO_2–RGO/ITO immunoelectrodes are repeatedly obtained.

And another control experiment was conducted to investigate the electrochemical response of APTES/ZrO_2–RGO/ITO electrode towards CYFRA-21-1 without using anti-CYFRA-21-1 (Fig. S9). We did not observe any significant changes in magnitude of the peak current with respect to different concentration of CYFRA-21-1. This result indicates that the sensor response is likely to be due to the immunoreaction between anti-CYRA-21-1 and CYFRA-21-1 molecules.

3.6. Interferents studies

Saliva is known to be saturated with a large number of organic, inorganic and biological analytes such as carcinoembroyonic antigen (CEA) [4–16 ng mL^{-1}], cardiac troponin I (CTN-I) [0.19 ng mL^{-1}], sodium carboxymethyl cellulose (NaCM) [10 mg mL^{-1}], glucose [7 mg mL^{-1}], endotheline 1 protein, NaCl (20 mM), $CaCl_2$ (1.13 mM), KCl (8.38 mM) etc. These analytes may interfere with the electrochemical response of a BSA/anti-CYFRA-21-1/APTES/ZrO_2–RGO/ITO immunoelectrode. To investigate the effect of these analytes on electrochemical response, we conducted the interferent studies (Fig. 4a) in PBS buffer (pH 7.0, 50 mM, 0.9% NaCl) containing $[Fe(CN)_6]^{3-/4-}$ (5 mM). First we added 2 ng mL^{-1} concentration of CYFRA-21-1. After a defined incubation time the peak current increased to 0.10 mA. On addition of the various analytes we observed that the maximum peak current change occurred in the presence of glucose and KCl with %RSD as 0.60% and 0.75% respectively. The mean %RSD due to all the interferents is 0.32% which is very low and has no significant effect on the peak current of electrochemical response. These results reveal that BSA/anti-CYFRA-21-1/APTES/ZrO_2–RGO/

Table 1
Determination of CYFRA-21-1 concentration in saliva samples using BSA/anti-CYFRA-21-1/APTES/ZrO_2–RGO/ITO bioelectrode.

S. No.	CYFRA-21-1 concentration determined using ELISA (in ng mL^{-1})	Peak current (mA) obtained for standard CYFRA-21-1 samples	Peak current samples (mA) obtained with saliva	%RSD (%)
1.	15.35	0.1095	0.1071	1.51
2.	13.35	0.1080	0.1035	3.35
3.	13.50	0.1082	0.1065	1.12
4.	14.15	0.1086	0.1048	2.52
5.	12.50	0.1074	0.1071	0.20
6.	14.15	0.1086	0.1053	2.18

ITO immunoelectrode is highly selective for the detection of CYFRA-21-1 antigen.

3.7. Real sample analysis

Enzyme linked immunosorbent assay (ELISA) was used for quantitative determination of CYFRA-21-1 in saliva samples of six oral cancer patients. We performed double-antibody sandwich ELISA in anti-CYFRA-21-1 coated 96 microtiter wells plate. Both the standard and the patient's samples were used in triplicate. Colorimetric reactions were recorded at 450 nm by ELISA plate reader (iMark, Bio red, USA). After determination of the CYFRA-21-1 concentration in the saliva of oral cancer patients by ELISA, the BSA/anti-CYFRA-21-1/APTES/ZrO_2–RGO/ITO electrode was used to record the DPV response towards different concentrations of the real samples. A reasonable agreement between the response current was obtained (Table 1) for real samples and the standard samples with acceptable %RSD. These results reveal high accuracy of the fabricated immunosensor for the determination of CYFRA-21-1 in clinical patient samples.

3.8. Stability and response time studies

The stability of the BSA/anti-CYFRA-21-1/APTES/ZrO_2–RGO/ITO immunoelectrode was determined by DPV studies at a regular interval upto 10 weeks (Fig. S10). The immunoelectrode was stored at 4 °C when not in use. It was observed that magnitude of the peak current exhibited 94% response upto 8 weeks after which the peak current decreased rapidly indicating that stability of the fabricated immunoelectrode is upto 8 weeks. The response time of the BSA/anti-CYFRA-21-1/APTES/ZrO_2–RGO/ITO immunoelectrode was determined by measuring DPV current response by varying the incubation period from 1 to 30 min (Fig. S11). It was found that the biosensor reached maximum peak current after 16 min of incubation revealing sufficient attachment of the antigens to the immonoelectrode surface. The sensing characteristics of the proposed BSA/anti-CYFRA-21-1/APTES/ZrO_2–RGO/ITO immunosensor are summarized in Table 2.

4. Conclusions

In summary, a non-invasive, label free and efficient immunosensor based on nanostructured zirconia decorated reduced graphene oxide has been fabricated to detect CYFRA-21-1 biomarker in saliva of oral cancer patients. The ZrO_2–RGO nanocomposite has been prepared through one step low temperature hydrothermal process and silanized with APTES. Further, the electrophoretic deposition (EPD) technique has been used for formation of the thin film of APTES/ZrO_2–RGO on ITO coated glass substrate. The APTES/ZrO_2–RGO/ITO electrode surface has been

Table 2
Characteristics of the various detection techniques used for oral cancer detection.

Method	Detection technique	Invasive/non-invasive	Label	Sample	Biomarker	Platform	Concentration range of biomarker	Sensitivity	Linear detection range	Response time	Shelf Life	Reference
Cytopathology	Staining	Invasive	–	Cells	–	–	–	–	–	–	–	Rosenberg and Cretin (1989)
Biopsy	Cell culture	Invasive	–	Tissue	–	–	–	–	–	2–3 Weeks	–	Patton et al. (2008)
Visualization adjuncts	Staining	Invasive	–	Tissue	–	–	–	–		1 Week	–	Patton et al. (2008)
Biosensor	Amperometric	Invasive	Yes	Serum	IL-6(Protein)	–	≤ 6 pg mL^{-1} to ≥ 20 pg mL^{-1}	19.3 nA mL pg^{-1} cm^{-2}	0.5–30 pg mL^{-1}	–	–	Malhotra et al. (2010)
	DPV	Invasive	Yes	Serum	IL-6 (Protein)	–	< 6 pg mL^{-1} to > 20 pg mL^{-1}	–	0.002–20 ng mL^{-1}	–	4 Weeks	Li and Yang (2011)
	CV	Non invasive	Yes	Saliva	has-miR-200a (miRNA)	–	–	–	1 aM–10 fM	–	–	Wang et al. (2013)
	CV	Non invasive	No	Saliva	CYFRA-21-1 (Protein)	BSA/anti-CYFRA-21-1/APTES/ZrO_2 /ITO	0–18 ng mL^{-1}	2.2 μA mL ng^{-1}	2–16 ng mL^{-1}	20 min	6 Weeks	Kumar et al. (2015b)
	DPV	Non invasive	No	Saliva	CYFRA-21-1 (Protein)	BSA/anti-CYFRA-21-1/APTES/ZrO_2–RGO/ITO	0–18 ng mL^{-1}	0.756 μA mL ng^{-1}	2–22 ng mL^{-1}	16 min	8 Weeks	Present work

functionalized with anti-CYFRA-21-1 antibodies and BSA molecules. The fabricated immunoelectrode (BSA/anti-CYFRA-21-1/APTES/ZrO_2–RGO/ITO) exhibits higher sensitivity (0.756 μ A mL ng^{-1}), wider linear detection range (2–22 ng mL^{-1}) and remarkable low detection limit (0.122 ng mL^{-1}). The shelf life of this immunoelectrode has been found to be 8 weeks and results of the sensing studies have been validated through ELISA. Efforts should be made to utilize this immunosensor for detection of other cancer biomarkers and it should be interesting to investigate the effect of the ZrO_2 nanoparticle and the role of antigen-antibody interactions on the performance of this immunosensor.

Acknowledgments

We thank Prof. Yogesh Singh, Vice Chancellor Delhi Technological University, Delhi (India) for providing the research facilities. We thank Dr. A.K. Dewan, Dr. D.C. Dovel and Dr. Birendra Kumar Yadav of Rajiv Gandhi Cancer Institute & Research Centre for valuable discussions. Suveen Kumar is thankful to DTU for the award of financial assistance, nanofabrication laboratry of DTU for the AFM facilities, Sandeep Mishra for XRD, Dr. Laxman S. Meena, Institute of Genomics and Integrative Biology, Delhi (India) for TEM studies and Dr. Saurabh Srivastava, Department of Applied Physics and Saroj Kumar, DTU for valuable scientific discussions.

Appendix A. Supplementary material

Supplementary data associated with this article can be found in the online version at http://dx.doi.org/10.1016/j.bios.2015.11.084.

References

Ali, M.A., Kamil Reza, K., Srivastava, S., Agrawal, V.V., John, R., Malhotra, B.D., 2014. Lipid–lipid interactions in aminated reduced graphene oxide interface for biosensing application. Langmuir 30 (14), 4192–4201.
Anusha, J., Kim, H.-J., Fleming, A.T., Das, S.J., Yu, K.-H., Kim, B.C., Raj, C.J., 2014. Simple fabrication of ZnO/Pt/chitosan electrode for enzymatic glucose biosensor. Sens. Actuators B: Chem. 202, 827–833.
Chen, J., Zhang, J., Guo, Y., Li, J., Fu, F., Yang, H.-H., Chen, G., 2011. An ultrasensitive electrochemical biosensor for detection of DNA species related to oral cancer based on nuclease-assisted target recycling and amplification of DNAzyme. Chem. Commun. 47 (28), 8004–8006.
Das, M., Dhand, C., Sumana, G., Srivastava, A., Vijayan, N., Nagarajan, R., Malhotra, B., 2011. Zirconia grafted carbon nanotubes based biosensor for M. Tuberculosis detection. Appl. Phys. Lett. 99 (14), 143702.
Dong, X.-C., Xu, H., Wang, X.-W., Huang, Y.-X., Chan-Park, M.B., Zhang, H., Wang, L.-H., Huang, W., Chen, P., 2012. 3D graphene–cobalt oxide electrode for high-performance supercapacitor and enzymeless glucose detection. ACS Nano 6 (4), 3206–3213.
Gong, J., Miao, X., Wan, H., Song, D., 2012. Facile synthesis of zirconia nanoparticles-decorated graphene hybrid nanosheets for an enzymeless methyl parathion sensor. Sens. Actuators B: Chem. 162 (1), 341–347.
Gonzalez, M., Artimez, M., Rodrigo, L., Lopez-Larrea, C., Menendez, M., Alvarez, V., Perez, R., Fresno, M., Perez, M., Sampedro, A., 1997. Mutation analysis of the p53, APC, and p16 genes in the Barrett's oesophagus, dysplasia, and adenocarcinoma. J. Clin. Pathol. 50 (3), 212–217.
Gorschinski, A., Khelashvili, G., Schild, D., Habicht, W., Brand, R., Ghafari, M., Bönnemann, H., Dinjus, E., Behrens, S., 2009. A simple aminoalkyl siloxane-mediated route to functional magnetic metal nanoparticles and magnetic nanocomposites. J. Mater. Chem. 19 (46), 8829–8838.
Guilbault, G.G., Palleschi, G., Lubrano, G., 1995. Non-invasive biosensors in clinical analysis. Biosens. Bioelectron. 10 (3), 379–392.
Kaushik, A., Solanki, P.R., Pandey, M., Ahmad, S., Malhotra, B.D., 2009. Cerium oxide-chitosan based nanobiocomposite for food borne mycotoxin detection. App. Phys. Lett. 95 (17), 173703.
Kujan, O., Glenny, A.M., Oliver, R., Thakker, N., Sloan, P., 2006. Screening Programmes for the Early Detection and Prevention of Oral Cancer. John Wiley & Sons, Ltd., The Cochrane Library, New York.
Kumar, S., Kumar, S., Srivastava, S., Yadav, B.K., Lee, S.H., Sharma, J.G., Doval, D.C., Malhotra, B.D., 2015a. Reduced graphene oxide modified smart conducting paper for Cancer biosensor Biosens. Bioelectron. 73, 114–122.
Kumar, S., Kumar, S., Tiwari, S., Srivastava, S., Srivastava, M., Yadav, B.K., Tran, T.T., Dewan, A.K., Mulchandani, A., Sharma, J.G., Maji, S., Malhotra, B.D., 2015b. Biofunctionalized nanostructured zirconia for biomedical application: a smart approach for oral cancer detection. Adv. Sci. 2 (8), 1500048.
Lawrence, H.P., 2002. Salivary markers of systemic disease: noninvasive diagnosis of disease and monitoring of general health. J. Can. Dent. Assoc. 68 (3), 170–175.
Li, T., Yang, M., 2011. Electrochemical sensor utilizing ferrocene loaded porous polyelectrolyte nanoparticles as label for the detection of protein biomarker IL-6. Sensors and Actuators B: Chemical 158 (1), 361–365.
Liu, G., Lin, Y., 2005. Electrochemical sensor for organophosphate pesticides and nerve agents using zirconia nanoparticles as selective sorbents. Anal. Chem. 77 (18), 5894–5901.
Malhotra, R., Patel, V., Vaqué, J.P., Gutkind, J.S., Rusling, J.F., 2010. Ultrasensitive electrochemical immunosensor for oral cancer biomarker IL-6 using carbon nanotube forest electrodes and multilabel amplification. Anal. Chem. 82 (8), 3118–3123.
Malhotra, R., Patel, V., Chikkaveeraiah, B.V., Munge, B.S., Cheong, S.C., Zain, R.B., Abraham, M.T., Dey, D.K., Gutkind, J.S., Rusling, J.F., 2012. Ultrasensitive detection of cancer biomarkers in the clinic by use of a nanostructured microfluidic array. Anal. Chem. 84 (14), 6249–6255.
Mehrotra, R., Gupta, D.K., 2011. Exciting new advances in oral cancer diagnosis: avenues to early detection. Head Neck Oncol. 3 (1), 1–9.
Nagler, R., Bahar, G., Shpitzer, T., Feinmesser, R., 2006. Concomitant analysis of salivary tumor markers—a new diagnostic tool for oral cancer. Clin. Cancer Res. 12 (13), 3979–3984.
Okuno, J., Maehashi, K., Kerman, K., Takamura, Y., Matsumoto, K., Tamiya, E., 2007. Label-free immunosensor for prostate-specific antigen based on single-walled carbon nanotube array-modified microelectrodes. Biosens. Bioelectron 22, 2377–2381.
Pasternack, R.M., Rivillon Amy, S., Chabal, Y.J., 2008. Attachment of 3-(aminopropyl) triethoxysilane on silicon oxide surfaces: dependence on solution temperature. Langmuir 24 (22), 12963–12971.
Patton, L.L., Epstein, J.B., Kerr, A.R., 2008. Adjunctive techniques for oral cancer examination and lesion diagnosis: a systematic review of the literature. J. Am. Dent. Assoc. 139 (7), 896–905.
Pickering, V., Jordan, R.C., Schmidt, B.L., 2007. Elevated salivary endothelin levels in oral cancer patients—a pilot study. Oral Oncol. 43 (1), 37–41.
Punyani, S.R., Sathawane, R.S., 2013. Salivary level of interleukin-8 in oral precancer and oral squamous cell carcinoma. Clin. Oral Investig. 17 (2), 517–524.
Rajkumar, K., Ramya, R., Nandhini, G., Rajashree, P., Ramesh Kumar, A., Nirmala Anandan, S., 2015. Salivary and serum level of CYFRA 21-1 in oral precancer and oral squamous cell carcinoma. Oral Dis. 21 (1), 90–96.
Roushani, M., Valipour, A., 2016. Using electrochemical oxidation of Rutin in modeling a novel and sensitive immunosensor based on Pt nanoparticle and graphene–ionic liquid–chitosan nanocomposite to detect human chorionic gonadotropin. Sens. Actuators B: Chem. 222, 1103–1111.
Sawangphruk, M., Srimuk, P., Chiochan, P., Krittayavathananon, A., Luanwuthi, S., Limtrakul, J., 2013. High-performance supercapacitor of manganese oxide/reduced graphene oxide nanocomposite coated on flexible carbon fiber paper. Carbon 60, 109–116.
Scully, C., Bagan, J.V., Hopper, C., Epstein, J.B., 2008. Oral cancer: current and future diagnostic techniques. Am. J. Dent. 21 (4), 199–209.
Sharma, A., Pandey, C.M., Sumana, G., Soni, U., Sapra, S., Srivastava, A., Chatterjee, T., Malhotra, B.D., 2012. Chitosan encapsulated quantum dots platform for leukemia detection. Biosens. Bioelectron. 38 (1), 107–113.
Solanki, P.R., Kaushik, A., Agrawal, V.V., Malhotra, B.D., 2011. Nanostructured metal oxide-based biosensors. NPG Asia Mater. 3 (1), 17–24.
Srivastava, S., Kumar, V., Ali, M.A., Solanki, P.R., Srivastava, A., Sumana, G., Saxena, P. S., Joshi, A.G., Malhotra, B., 2013. Electrophoretically deposited reduced graphene oxide platform for food toxin detection. Nanoscale 5 (7), 3043–3051.
Tille, P., 2013. Bailey & Scott's Diagnostic Microbiology. Elsevier Health Sciences, United States.
Vasudev, A., Kaushik, A., Bhansali, S., 2013. Electrochemical immunosensor for label free epidermal growth factor receptor (EGFR) detection. Biosens. Bioelectron. 39 (1), 300–305.
Vilian, A.E., Chen, S.-M., Huang, L.-H., Ali, M.A., Al-Hemaid, F.M., 2014. Simultaneous determination of catechol and hydroquinone using a Pt/ZrO 2-RGO/GCE composite modified glassy carbon electrode. Electrochim. Acta 125, 503–509.
Viswanathan, S., Wu, L.C.M., Huang, R., Ho, J.A., 2006. Electrochemical immunosensor for cholera toxin using liposomes and poly(3,4-ethylenedioxythiophene)-coated carbon nanotubes. Anal. Chem. 78, 1115–1121.
Wan, Y., Su, Y., Zhu, X., Liu, G., Fan, C., 2013. Development of electrochemical immunosensors towards point of care diagnostics. Biosens. Bioelectron. 47, 1–11.
Wang, J.H., Wang, B., Liu, Q., Li, Q., Huang, H., Song, L., Sun, T.Y., Wang, H., Yu, X.F., Li, C., 2013. Bimodal optical diagnostics of oral cancer based on Rose Bengal conjugated gold nanorod platform. Biomaterials 34 (17), 4274–4283.
Wei, J., Qiu, J., Li, L., Ren, L., Zhang, X., Chaudhuri, J., Wang, S., 2012. A Reduced graphene oxide based electrochemical biosensor for tyrosine detection. Nanotechnology 23 (33), 335707.
Wei, Y., Gao, C., Meng, F.-L., Li, H.-H., Wang, L., Liu, J.-H., Huang, X.-J., 2011. SnO_2/reduced graphene oxide nanocomposite for the simultaneous electrochemical detection of cadmium (II), lead (II), copper (II), and mercury (II): an interesting favorable mutual interference. J. Phys. Chem. C 116 (1), 1034–1041.
Zhang, S., Zheng, F., Wu, Z., Shen, G., Yu, R., 2008. Highly sensitive electrochemical detection of immunospecies based on combination of Fc label and PPD film/gold nanoparticle amplification. Biosens. Bioelectron 24, 129–135.
Zhao, N., Pan, D., Nie, W., Ji, X., 2006. Two-phase synthesis of shape-controlled colloidal zirconia nanocrystals and their characterization. J. Am. Chem. Soc. 128 (31), 10118–10124.